ACS NANO

www.acsnano.org

Integrated Computational and Experimental Framework for Inverse Screening of Candidate Antibacterial Nanomedicine

Jia-Jia Zheng,[†] Xiaoyu Wang,[†] Zeqi Li,[†] Xiaomei Shen, Gen Wei, Pufeihong Xia, Yi-Ge Zhou,* Hui Wei,* and Xingfa Gao*

Cite This: https://doi.org/10.1021/acsnano.3c09128

Read Online

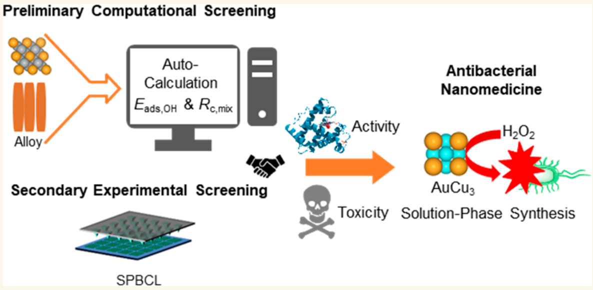

ABSTRACT: **Nanomedicine is promising for disease prevention and treatment, but there are still many challenges that hinder its rapid development. A major challenge is to efficiently seek candidates with the desired therapeutic functions from tremendously available materials. Here, we report an integrated computational and experimental framework to seek alloy nanoparticles from the Materials Project library for antibacterial applications, aiming to learn the inverse screening concept from traditional medicine for nanomedicine. Because strong peroxidase-like catalytic activity and weak toxicity to normal cells are the desired material properties for antibacterial usage, computational screening implementing theoretical prediction models of catalytic activity and cytotoxicity is first conducted to select the candidates. Then, experimental screening based on scanning probe block copolymer lithography is used to verify and refine the computational screening results. Finally, the best candidate $AuCu_3$ is synthesized in solution and its antibacterial performance over other nanoparticles against *S. aureus* and *E. coli.* is experimentally confirmed. The results show the power of inverse screening in accelerating the research and development of antibacterial nanomedicine, which may inspire similar strategies for other nanomedicines in the future.**

KEYWORDS: *alloy nanoparticles, antibacterial nanomedicine, density functional theory calculations, inverse screening, nanozymes*

INTRODUCTION

Nanomedicine refers to the application of engineered nanomaterials for disease prevention and treatment.[1−3] Nanomaterials possess versatile chemical compositions, structures, tunable physicochemical properties, and functionalities, which enable them to potentially overcome the drawbacks commonly associated with conventional small molecular drugs, such as high dosage, poor targeting, severe toxicity, side effects, and susceptibility to drug resistance. These advantages suggest that it is promising to significantly improve the curative effects and reduce healthcare costs through the application of nanotechnology for medical care. Consequently, nanomedicine is of high research value and is expected to have broad market prospects in the coming decade.[4,5] Recent studies have demonstrated that nanomaterials are promising alternatives to conventional antibiotics. Owing to their versatile antibacterial mechanisms, including membrane destruction, disruption of the electron transport chain, catalytic killing, cell division arrest, prolonged ionic killing and aggregation-mediated cell trapping, nanomaterials are potentially free to antimicrobial resistance.[6−8] For instance, nanomaterials possessing peroxidase-like (POD-like) catalytic activity can catalyze the decomposition of H_2O_2 to produce highly toxic hydroxyl groups and trigger the bacterial death by the oxidation of cellular substance (electron donor, eq 1), serving as potential nanomedicine to prevent bacterial infection.[8−13] Intriguingly, because it combats bacterial in a manner that differs from conventional antibiotics[14] by disrupting the cell membrane integrity and damaging bacterial DNA and intracellular proteins through the production of highly oxidative hydroxyl groups,[8,13] this catalysis-enabled antibacterial nanomedicine is promising to overcome antimicrobial resistance, which is becoming a huge threat to humanity.[15]

Received: September 21, 2023
Revised: December 21, 2023
Accepted: December 22, 2023

However, a tremendous number of nanomaterials have been fabricated so far, making it extremely difficult to precisely seek targets with desired medical functions such as antibacterial activity, which significantly hinders the further development of nanomedicine.

$$H_2O_2 + 2H^+ + 2\text{donor} \xrightarrow{\text{POD}} 2H_2O + 2\text{ox} - \text{donor} \quad (1)$$

Computer-aided inverse screening, which discovers molecules with predefined therapeutic properties, has become an indispensable technique to cost-effectively develop drugs.[16] This technique has successfully brought several compounds into the medicine market, including dorzolamide in 1995,[17] nelfinavir in 1997,[18] and relenza in 1999,[19] demonstrating its power in seeking promising candidates from the mass molecular libraries. In addition, this technique has successfully accelerated discovery of nanomaterials for CO_2 reduction,[20] solar cell,[21] nitrogen fixation,[22] and so on. With the development of more powerful computer hardware and artificial intelligence algorithms, such an inverse screening method is believed to play more important roles in the modern pharmaceutical industry. Therefore, it is highly desirable to learn the inverse screening technique from traditional medicine for nanomedicine.

Here, we report the construction and validation of an integrated computational and experimental framework for inverse screening of alloy nanoparticles from the Materials Project library[23,24] toward antibacterial nanomedicine (Figure 1). We are interested in alloy nanoparticles because of their various advantages, such as unique electronic structures, ordered atomic structures, diverse atomic sizes, thermodynamic stability, and expandability, all of which may enhance the catalytic capacity of intermetallic materials.[25] Strong POD-like catalytic activity and weak cytotoxicity to normal cells, which benefit antibacterial applications, are defined as the properties for screening. Briefly, the POD-like activity model,[26−28] which was recently proposed by our group to predict the POD-like catalytic activity of material surfaces, is verified for alloys. The verified model can then be interfaced with the Materials Project library to screen binary alloys possessing POD-like activity from those made of 3d−5d transition metals (TMs). The cytotoxicity of the alloys is evaluated using the nano-QSAR model[29−31] to exclude those toxic to normal cells. After these two steps of computational screening, scanning probe block copolymer lithography (SPBCL) is employed to fabricate highly uniform metal and alloy nanoparticles for secondary experimental screening. Through the combined computational and experimental screening, $AuCu_3$ is suggested as the best candidate in terms of the catalytic activity and safety. The antibacterial activity of $AuCu_3$ prepared by the wet-chemistry strategy is tested by plate count experiments, supporting the reliability of the inverse screening technique. The results discover the $AuCu_3$ alloy as a potential antibacterial nanomedicine without antimicrobial resistance. Meanwhile, they prove the significant role of inverse screening in promoting the research of antibacterial nanomedicine, which may also inspire the research of other nanomedicine in the future.

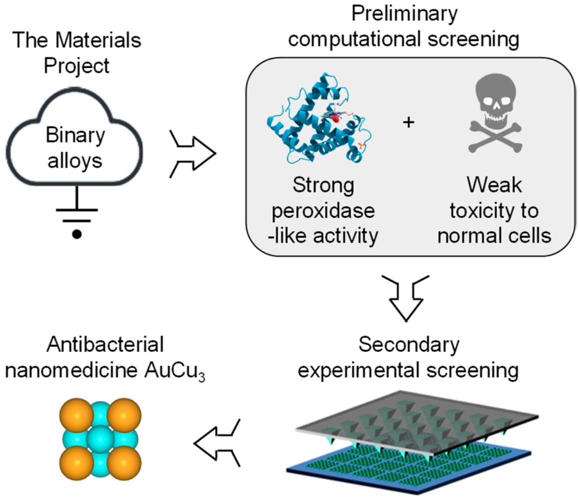

Figure 1. Schematic representation of an integrated computational and experimental framework for inverse screening of antibacterial nanomedicine.

RESULTS AND DISCUSSION

Validation of POD-like Activity Model for Alloys. Because the antibacterial function of nanomaterials is substantialized by their POD-like catalytic activity,[8−13] a reliable prediction of the catalytic activity is essential to enable the inverse screening of the nanomedicine. Here, the POD-like catalytic activity of nanomaterials was assessed by the reaction of H_2O_2 with 3,3′,5,5′-tetramethylbenzidine (TMB), which was the same as previous studies (Figure 2a).[32,33] We have recently proposed a theoretical model to predict the relative POD-like catalytic activities of a single active site of material surfaces for this prototype reaction.[26] As shown in Figure 2b, this model is based on the hydroxyl (OH) adsorption energy ($E_{\text{ads,OH}}$) on a given nanosurface. This model indicates that too weak hydroxyl adsorption impedes the decomposition of H_2O_2, while too strong hydroxyl adsorption hinders the oxidation of substrates. Therefore, there is an optimum $E_{\text{ads,OH}}$ value, which was found to be −2.60 eV, to achieve the highest POD-like activity of nanomaterials. In addition, the POD-like activity window has been defined as $-3.50\text{ eV} < E_{\text{ads,OH}} < -1.60\text{ eV}$,[26] and the optimal activity window has been defined as $-2.80\text{ eV} < E_{\text{ads,OH}} < -2.40\text{ eV}$. With this POD-like activity model, it is convenient to predict whether a nanomaterial can be considered as a POD mimic by calculating the $E_{\text{ads,OH}}$ without studying the entire reaction process. This model has been successfully applied to understand the better POD-like activity of the Mo/Zn dual-site nanoparticle than the corresponding single-site ones.[34]

Because it does not consider sizes and morphologies of nanoparticles, the POD-like activity model is applicable only to describe the relative capacity of nanoparticles that have similar sizes and morphologies. To verify whether the POD-like activity model is adoptable for metallic nanomaterials, we compared the experimentally reported POD-like activities of several noble metals (Ru, Pd, Ir, Au, and Pt) with respect to their $E_{\text{ads,OH}}$ values. As shown in Figure 2b and Table S1, $E_{\text{ads,OH}}$ values for Pd, Ir, and Pt are very close to the optimal one, which is consistent with their good POD-like activities, as reported in experiments.[35−37] On the other hand, the $E_{\text{ads,OH}}$ values for Ru and Au are too strong (−3.70 eV for Ru) or too weak (−2.20 eV for Au), resulting in their weaker POD-like activities[38,39] than those of Pd, Ir, and Pt.[35−37] These results validate that our prediction model for the POD-like activity of nanomaterials on the basis of $E_{\text{ads,OH}}$ can also be applied to metallic nanomaterials.

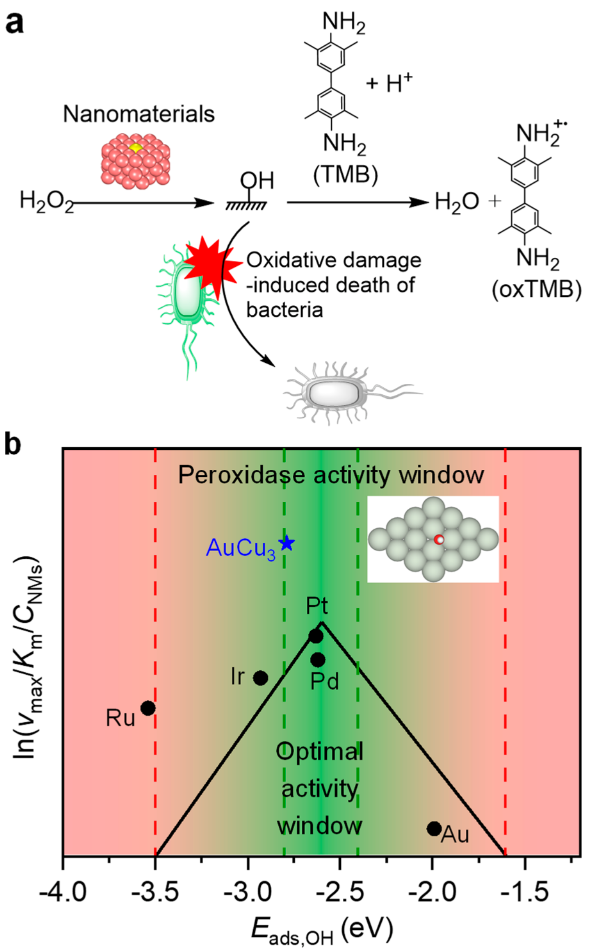

Figure 2. Validation of the peroxidase-like activity model. a) Prototype reaction for evaluating the peroxidase-like catalytic activity underling antibacterial function of nanomaterials. b) Theoretical model based on hydroxyl adsorption energy ($E_{ads,OH}$) to predict the peroxidase-like catalytic activity of material surfaces. The peroxidase like-activity window was found to be −3.50 eV < $E_{ads,OH}$ < −1.60 eV and the optimal activity window was −2.80 eV < $E_{ads,OH}$ < −2.40 eV. $AuCu_3$ is the alloy screened out from the materials project library.

Preliminary Computational Screening. To find medically applicable alloy nanomaterials with high POD-like activity and low cytotoxicity, we constructed a computational screening framework to interface with the Materials Project,[23,24] a publicly available materials library. The possible binary alloys in the library consisting of 3d to 5d TMs without Hg were queried, during which only the stable or experimentally observed structures ("is_stable = True" or "theoretical = False") were considered, leading to a total of 844 binary alloys (Figure 3a). Some of these alloys contain many metal sites, which are very difficult for the DFT calculations. Therefore, we further reduced the number of samples by considering only those alloys that are nonmagnetic ("is_magnetic = False") and small in size (nsites ≤ 4). Finally, 260 binary alloys were considered in the computational inverse screening of POD-like activity (Table S2). Next, a workflow was constructed for autocalculation of $E_{ads,OH}$ on different surfaces of alloys (Figure 3b). The crystal structure of an alloy was obtained with its ID in the Materials Project (mp-ID) and then optimized using the DFT method. The optimized crystal structure was then employed to construct different exposed surfaces, for which only surfaces with Miller indices between −1 and 1, such as the (100), (110), and (111) surfaces, were considered. For unsymmetrical top and bottom surfaces, both of them were considered. This resulted in a total of 1700 unique surfaces for 260 binary alloys. These surfaces were then used to generate OH adsorption structures, and further DFT calculations were performed to obtain $E_{ads,OH}$. For convenience of discussion, these surfaces will be denoted as $^{\text{mp-ID}}$formula-*hkl*, where mp-ID is the ID of an alloy in the Materials Project, formula is the composition of elements in an alloy, and *hkl* is the Miller indices for a specific surface.

The distribution of DFT-calculated $E_{ads,OH}$ for all the 1700 surfaces is shown in Figure S1. Although most of these surfaces have too strong OH affinity, there are 353 candidates (21.8%) falling into the POD-like activity window, as can be seen in Figure 3c, suggesting that it is promising to discover strong POD-like catalytic activities in these TM alloy nanomaterials. In order to recognize the proper alloy nanomaterials for antibacterial applications, we further examined the surfaces that are ideal for POD-mimics. These surfaces are mainly composed of noble metals such as Ag, Au, Pd, and Pt, which is not surprising because these metals have moderate $E_{ads,OH}$ values that do not deviate much from the optimal value −2.6 eV for mimicking POD. Interestingly, the POD-like activity of alloy nanoparticles consisting of Au, Ag, and Cu was also reported in experiment,[40] which again suggests the availability of our prediction model in finding POD-mimicking alloys. It is worth noting that there are six ideal POD-mimicking surfaces containing the earth-abundant element Cu, namely, $^{\text{mp-2258}}$AuCu$_3$-100, $^{\text{mp-522}}$AuCu-100, $^{\text{mp-522}}$AuCu-111, $^{\text{mp-2103}}$Au$_3$Cu-100, $^{\text{mp-2103}}$Au$_3$Cu-110, and $^{\text{mp-2103}}$Au$_3$Cu-111 (Figure 3d). It should be noted that the $E_{ads,OH}$ values for different exposed surfaces of $AuCu_3$ differ very much; the (100) surface exposing both Cu and Au atoms is ideal to show the peroxidase-like activity, and other surfaces have too attractive affinities to the hydroxyl group, suggesting the morphology-dependent peroxidase-like activity of nanomaterials. Compared to the Au_yCu_x alloys, alloys of Cu with other noble metals are either unstable (such as Ag_xCu_y) or more attractive to the OH (such as Cu_xPd_y and Cu_xPt_y), making them unsuitable as ideal POD mimics. Given that the OH affinity decreases in the order of Au < Pt < Pd ≈ Ag < Cu, these results suggest that alloying a weakly attractive metal with a strongly attractive metal or two moderately attractive metals can lead to better POD-like activities than the metals alone. Similar trends are also observed for alloys containing Cd and Zn, of which 13 surfaces are predicted to be ideal POD mimics.

In addition to POD-like catalytic activity, cytotoxicity of nanomaterials is another property to be considered for their application as antibacterial medicine. Several descriptors based on the physical properties of nanomaterials have been proposed to evaluate the cytotoxicity of metals and metal oxides using the nano-QSAR model.[29−31] Among those reported descriptors, periodic table-based physical properties, such as covalent radius (R_c)[31] and absolute electronegativity (μ),[30] are very useful in the computational inverse screening due to the avoidance of extensive calculations. In our screening framework, we selected R_c as the descriptor for the cytotoxicities of alloys, represented by pEC50 (see Methods), because it is able to well describe the order in cytotoxicities of Ag and Au nanoparticles (Table S3). Figure 4 shows the predicted cytotoxicities of various alloys with high POD-like activities; see Table S2 for cytotoxicities of all alloys

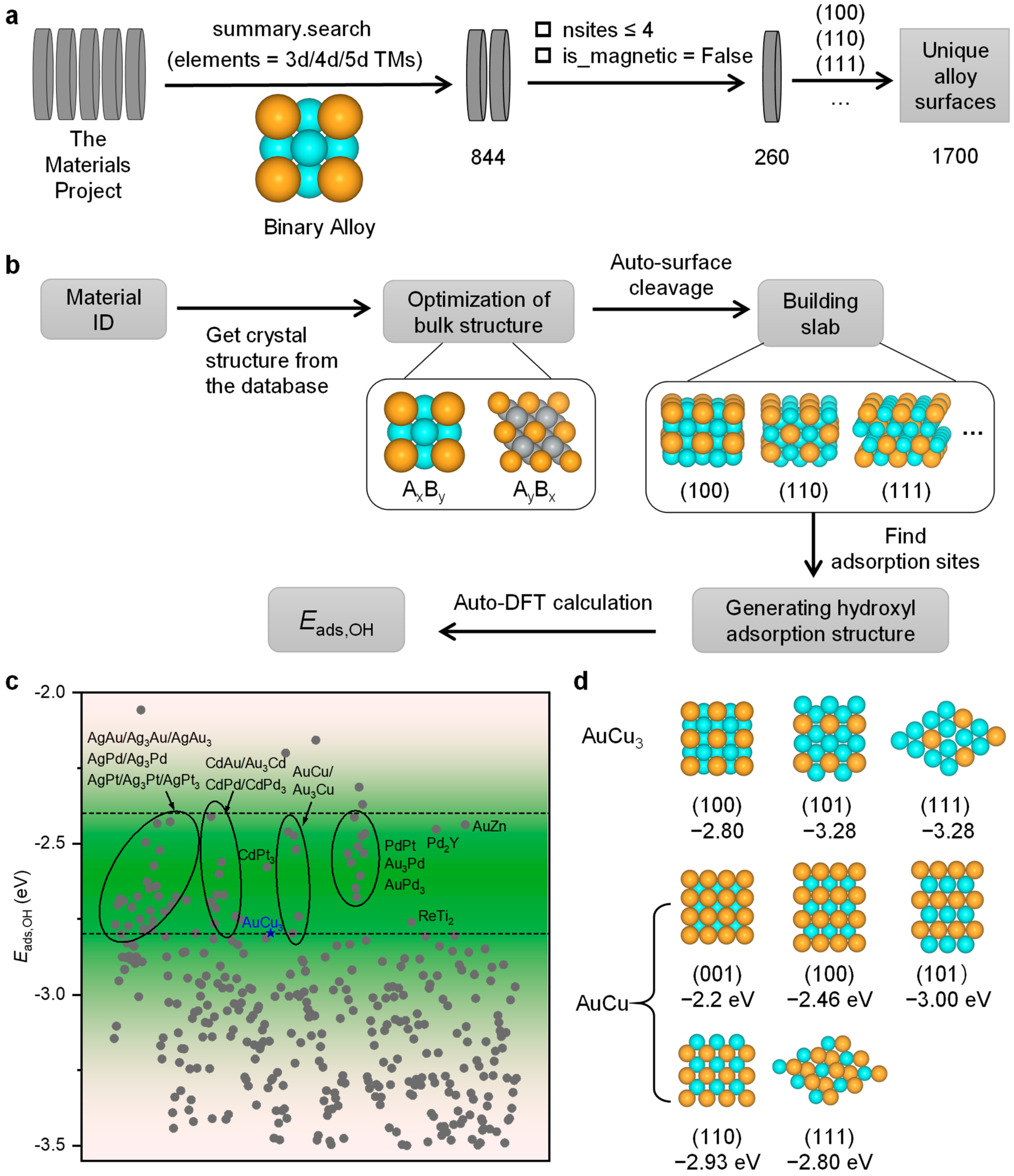

Figure 3. Computational screening of peroxidase-like alloys. (a) Schematic representation for alloy search and selection from the Materials Project. (b) Workflow for high-throughput DFT calculations of $E_{ads,OH}$, including autoconstruction of structures and autocalculations. (c) DFT-revealed surfaces with hydroxyl adsorption energy $E_{ads,OH}$ falling into the peroxidase-activity window (−3.50 eV, −1.60 eV). (d) Surfaces of $^{mp\text{-}2258}AuCu_3$ and $^{mp\text{-}522}AuCu$ along with their $E_{ads,OH}$ values.

investigated in this work. Alloys containing early TMs such as Ti_2Re and YPd_2 are the most toxic among the ideal POD-like alloys because of their larger R_c values. For a similar reason, Ag- and Cd-containing alloys show larger cytotoxicities than Au-containing ones, which is consistent with our general understanding of the toxicities of these metallic nanoparticles. Interestingly, alloys consisting of Au and Cu, such as $AuCu_3$, AuCu, and Au_3Cu, are among the least toxic alloys with moderately lower toxicity than pure Au (pEC50 = 5.53), suggesting that the incorporation of Cu into Au nanoparticles does not have a significant effect on the cytotoxicity. These results demonstrate the power of our inverse screening framework, which reveals a series of safe and inexpensive alloys ($AuCu_3$ and AuCu) with high POD-like catalytic activities, suggesting their potential in antibacterial application.

Secondary Experimental Screening. To verify whether the Cu-containing alloys predicted in the preliminary computational inverse screening are excellent POD-mimics, we performed secondary experimental screening by producing highly uniform nanoparticles and testing their POD-like

https://doi.org/10.1021/acsnano.3c09128
ACS Nano XXXX, XXX, XXX−XXX

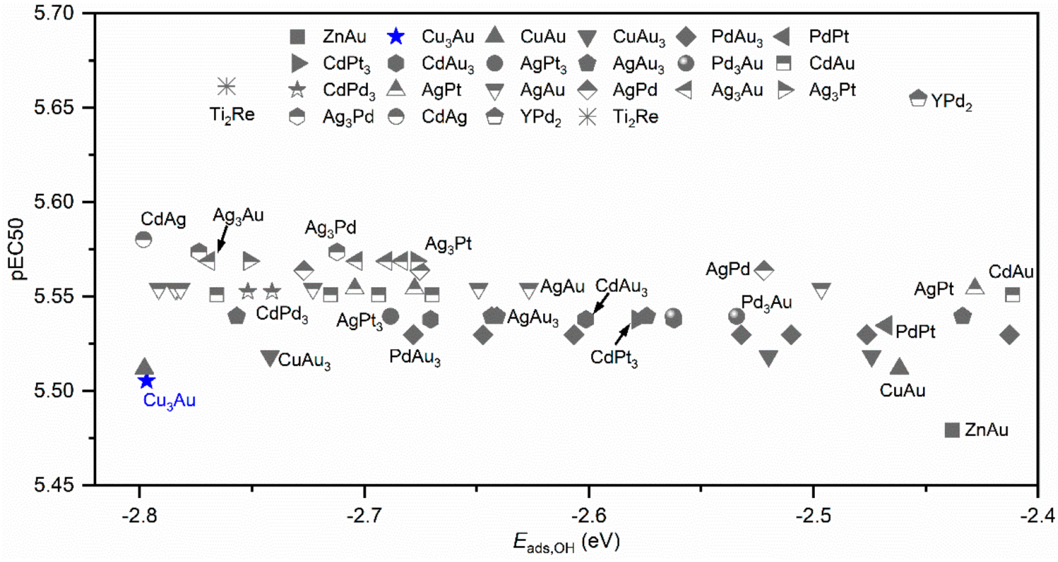

Figure 4. Cytotoxicity (pEC50) predicted for alloys with the nano-QSAR model. Only alloys with hydroxyl adsorption energy ($E_{ads,OH}$) located in the optimal activity zone (−2.4 ∼ −2.8 eV), namely, those predicted to have strong POD-like activity, are considered in the figure.

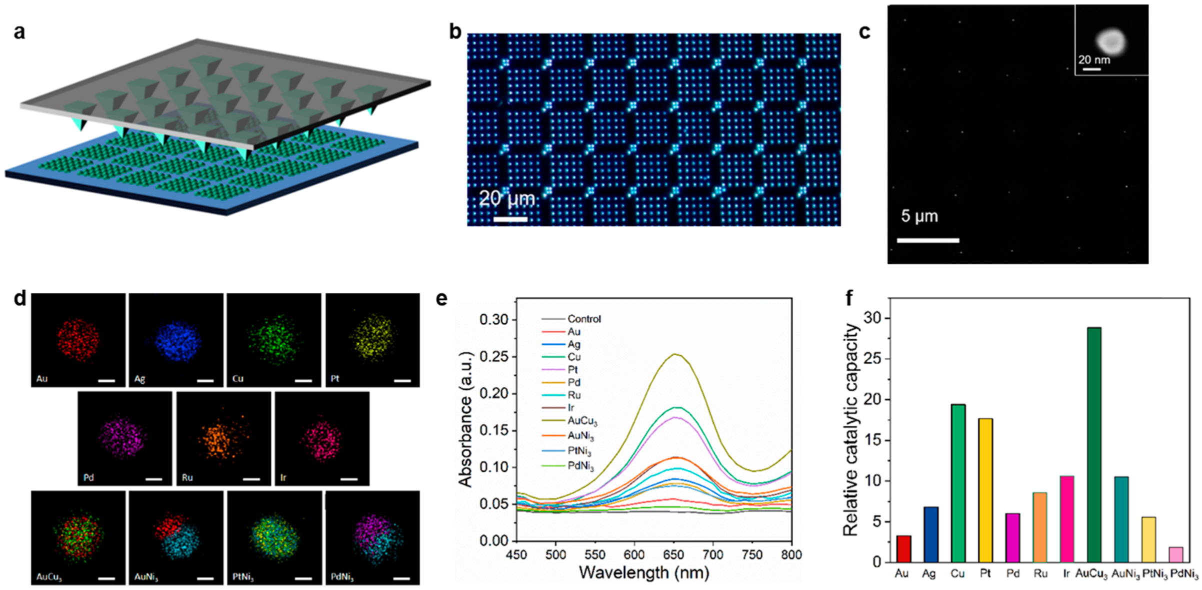

Figure 5. Screening of peroxidase-like alloys with scanning probe block copolymer lithography. (a) Schematic diagram of patterning process. (b) Optical microscopic image of nanoreactor arrays printed on the hexamethyl disilazane modified silicon wafer. (c) Scanning electron microscope image of the obtained Au nanoparticle array. Inset showing a zoomed-in detail of a representative nanoparticle. (d) Elemental mapping of the multimetallic nanoparticle library. Scale bar: 10 nm. (e) Typical absorption spectra of 0.5 mM TMB after catalytic oxidation with 100 mM H_2O_2 in pH 4.5 acetate buffer in the presence of various nanoparticle arrays. (f) Histograms comparing the relative catalytic capacity of metal and alloys. An error bar in the relative catalytic capacity was absent, because the standard deviation is small for selected nanoparticles (Au, Cu, Pt, Ir, and AuCu$_3$, Figure S3).

activities. For comparison, several noble metals and Ni-containing alloys were also considered. In order to obtain well-defined model systems in the study of their POD-like activities, SPBCL[41−44] was employed to produce metal and alloy nanoparticles (Figure 5). Compared to solution phase synthesis, SPBCL is a surfactant/stabilizer-free approach and in the meantime can overcome common aggregation problems. Moreover, the resulting nanoparticle arrays prepared using SPBCL exhibit similar sizes and morphologies, as well as comparable numbers of catalytically active sites, allowing for a precise investigation of the structure−activity relationship of the nanoparticles.[45] Therefore, SPBCL nanoparticle arrays can serve as an ideal model system for the experimental screening of POD-mimicking alloys.

The patterning process of the nanoreactors is illustrated in Figure 5a, which appear to be uniform arrays by optical microscopic observation (Figure 5b). The polymetallic nanoparticles could be obtained by a two-step annealing process. To confirm the formation of a single nanoparticle in each nanoreactor, the prepared Au nanoparticles was characterized by scanning electron microscope (SEM). Figure 5c shows a representative result. It can be observed that more than 80% of the nanoreactors can form single nanoparticles. In addition, a narrow size distribution of 28−32 nm was obtained, indicating

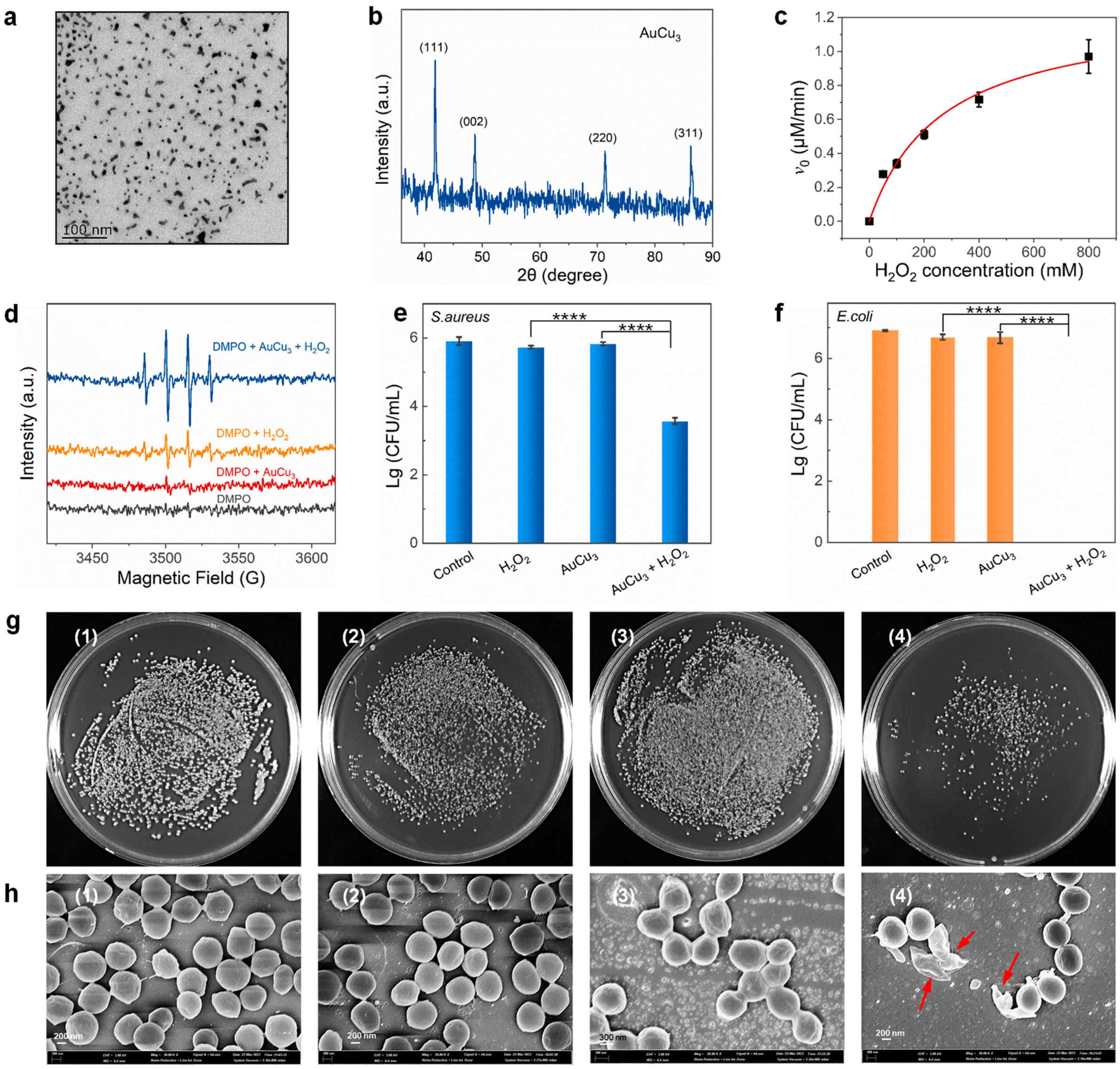

Figure 6. Wet-chemistry synthesis of AuCu$_3$ and antibacterial test. (a) TEM image of AuCu$_3$ nanoparticles. (b) Powder X-ray diffraction pattern of AuCu$_3$ nanoparticles. (c) Plots of the initial reaction velocity of AuCu$_3$ nanoparticles as a function of H_2O_2 concentration (1 mM of TMB). Each error bar shows the standard deviation of three independent measurements. (d) ESR spectra of DMPO mediated by 10 μg/mL of AuCu$_3$, 100 μM of H_2O_2, and 10 μg/mL of AuCu$_3$ + 100 μM of H_2O_2. (e, f) Antibacterial activity of AuCu$_3$ (10 μg/mL)/H_2O_2 on Gram-positive *S. aureus* and Gram-negative *E. coli*. For *S. aureus*, $[H_2O_2] = 50$ μM; for *E. coli*, $[H_2O_2] = 100$ μM. (g) Photographs of *S. aureus* colonies after different treatments. (h) Representative SEM images of *S. aureus* after different treatments with arrows indicating the disrupted bacteria. Cultured bacteria were treated with (1) NaAc-HAc buffer (control), (2) 50 μM H_2O_2, (3) 10 μg/mL AuCu$_3$, and (4) 10 μg/mL AuCu$_3$ + 50 μM of H_2O_2. All data are taken as mean ± s.d. ($n = 3$). Statistical significance was performed by a two-tailed Student's *t* test. ****$P < 0.0001$. The concentration of H_2O_2 was fixed at 100 and 50 μM for *E. coli* and *S. aureus*, respectively, because they have different susceptibilities to H_2O_2.

good uniformity of the SPBCL-synthesized nanoparticles. To examine the elemental distribution of the nanoparticles, spherical aberration corrected transmission electron microscope (AC-TEM) was performed, as shown in Figure 5d, where AuCu$_3$ and PtNi$_3$ nanoparticles exhibit alloy structures, while AuNi$_3$ and PdNi$_3$ nanoparticles are phase-separated heterostructures. These observations reflect the miscibility of the metal components.[44]

To evaluate the POD-like activities of nanoparticle arrays, absorption spectroscopy was used to monitor the catalytic oxidation of TMB, a typical POD substrate, with H_2O_2 in the presence of metal and alloy nanoparticles (Figure S2). As shown in Figure 5e, 5f and S3, the order in the POD-like activities of metal and alloy nanoparticles is in general agreement with the results predicted by the computational inverse screening. Moreover, among these metal and alloy nanoparticle arrays, AuCu$_3$ exhibited the highest POD-like activity, which is consistent with the computational results. Therefore, the combined computational and experimental inverse screening indicates that AuCu$_3$ is an excellent POD-mimic that is expected to be useful for antibacterial applications.

Wet-Chemistry Synthesis and Antibacterial Test. Although the high POD-like activity of AuCu$_3$ has been demonstrated by computational and experimental inverse screening, for practical applications, nanoparticles dispersed in the solution phase must be obtained for potential antibacterial usage. Therefore, we synthesized $AuCu_3$ nanoparticles by a typical one-step coreduction method[46] to verify the antibacterial performances of $AuCu_3$. Copper acetate and gold chloride were reduced at the same time in the presence of sodium borohydride, and the solution color gradually changed from dark red to dark brown, suggesting the formation of Au and Cu composite particles. Atomically ordered $AuCu_3$ alloy nanoparticles could be obtained by annealing a mixture of Au and Cu nanoparticles under an inert atmosphere. Figures 6a and S4 show the typical transmission electron microscope (TEM) images of $AuCu_3$ alloy nanoparticles. Although the size of $AuCu_3$ nanoparticles prepared by the wet-chemistry method was smaller than SPBCL-synthesized nanoparticles, we anticipate that the $AuCu_3$ nanoparticles would still exhibit good peroxidase-like activity. This is due to the fact that our computational screening considered only the composition that reflects the intrinsic catalytic capacity of nanomaterials. As shown in Figure 6b, all of the diffraction peaks of the sample are consistent with the $AuCu_3$ intermetallic phase.[46] The inductively coupled plasma atomic emission spectrometry (ICP-OES) analysis suggests a stoichiometry of $AuCu_{3.52}$ (Table S4), which is close to the ratio of precursors (Au: Cu = 1:3). As can be seen from the high-resolution (HRTEM) image (Figure S5), a lattice fringe spacing of 0.229 nm corresponds to $AuCu_3$ (111). The elemental mapping results suggested that Au and Cu were homogeneously distributed on the $AuCu_3$ nanoparticles (Figure S6). All of these results demonstrate the successful synthesis of $AuCu_3$ nanoparticles.

The POD-like activities of $AuCu_3$ nanoparticles were further explored. We quantified the catalytic efficiencies of $AuCu_3$ nanoparticles using apparent steady-state kinetic assays (Figure 6c and Figures S7 and S8). A typical Michaelis−Menten curve could be obtained by plotting the initial reaction velocities as a function of the H_2O_2 concentration (Figure 6c). The enzyme kinetic parameters, including the Michaelis−Menten constant (K_m) and the maximum initial velocity (v_{max}), could be calculated by converting the Michaelis−Menten curve into a double-reciprocal plot (Figure S8). As shown in Table S5, $AuCu_3$ nanoparticles exhibited high v_{max} values, further demonstrating their excellent POD-like activities. To confirm whether $AuCu_3$ nanoparticles could catalyze the decomposition of H_2O_2 to generate hydroxyl adsorbate (OH*) as the reactive intermediate, we first performed fluorescent assays using terephthalic acid (TA) as a fluorescent probe. TA could react with OH* to generate 2-hydroxy terephthalic acid (TAOH), which possessed a characteristic fluorescent signal at 435 nm. As shown in Figure S9, a characteristic signal that appeared with an emission peak at 435 nm could be observed upon the addition of H_2O_2 and $AuCu_3$ nanoparticles into the TA solution, indicating the formation of TAOH. Moreover, electron spin resonance spectra (ESR) were also used to directly demonstrate the generation of OH* by using 3,4-dihydro-2,2-dimethyl-2H-pyrrole1-oxide (DMPO) as an ESR spin-trapping agent. As shown in Figure 6d, a characteristic signal with a 1:2:2:1 line was produced in the presence of H_2O_2 and $AuCu_3$ nanoparticles, indicating the formation of the hydroxyl adduct of DMPO. These results verified that $AuCu_3$ nanoparticles could serve as excellent POD mimics for catalyzing the H_2O_2 to generate reactive OH*, making $AuCu_3$ nanoparticles promising antibacterial candidates because of their potential in inducing the bacterial programmed cell death by the oxidation of cellular substances.[8,13] We further evaluated the cytotoxicity of the $AuCu_3$ nanoparticles. The results show that the $AuCu_3$ is stable with a small amount of toxic Cu^{2+} released (Table S6) and that no notable cytotoxic effects on RAW 264.7 macrophages could be observed when the concentration of nanoparticles is below 50 μg/mL (Figure S10), demonstrating the good biocompatibility of $AuCu_3$ nanoparticles. The low cytotoxicity of $AuCu_3$ nanoparticles was consistent with the predicted results by calculations (Figure 4 and Figure S10).

Given that they could effectively catalyze H_2O_2 to exhibit POD-like catalytic activity, $AuCu_3$ nanoparticles were developed for antibacterial application. We evaluated the antibacterial effect of $AuCu_3$ nanoparticles against two representative bacteria, Gram-positive bacterium *S. aureus* and Gram-negative bacterium *E. coli*, by quantitative analysis using colony-forming units (CFU). We first incubated the bacterial solution with different groups for 3 h at 37 °C in an incubator shaker. After treatment, we used 20 μL of suspension to spread evenly on solid agar medium for CFU enumeration, and 100 μL of the above suspension was spread evenly on solid agar medium for taking photographs of colonies. As shown in Figure 6e−g and Figures S11 and S12, in the presence of a low concentration of H_2O_2 with 50 or 100 μM, as low as 10 μg/mL $AuCu_3$ nanoparticles could possess significant antibacterial activity against *S. aureus* and *E. coli*. The amounts of $AuCu_3$ and H_2O_2 required to achieve satisfactory antibacterial performance are much smaller than those of other POD-mimicking nanoparticles (Table S7), including Pt single-atom nanoparticles (250 μg/mL), oxygenated-group-enriched carbon nanotubes (100 μg/mL), Copper/carbon nanoparticles (250 μg/mL), and monodispersed ZIF-8 derived carbon nanospheres with a zinc-centered porphyrin-like structure (PMCs, 100 μg/mL). These results suggest the superior antibacterial properties of $AuCu_3$ over those of other nanoparticles. On the other hand, $AuCu_3$ nanoparticles or H_2O_2 alone exhibited weak antibacterial activity (Figures 6e−g and Figures S11 and S12), suggesting the low cytotoxicity of $AuCu_3$ nanoparticles, as predicted in the computational inverse screening. It is interesting to note that the cellular survival percentages differ upon exposure to 10 μg/mL $AuCu_3$ nanoparticles. Macrophages showed a survival percentage of approximately 95% (Figure S10), whereas bacteria had a survival percentage of around 65−85% (Figure S11). This difference may be attributed to the different susceptibilities of bacteria and mammalian cells to $AuCu_3$ nanoparticles, influenced by their different biological contexts, such as H_2O_2 concentration. In addition, the weak antibacterial activity of $AuCu_3$ nanoparticles alone suggests that mechanical stress exerted by the nanoparticles is not enough to induce bacterial death. SEM characterization was further performed to observe the bacterial morphology with different treatments. As shown in Figure 6h and Figure S13, the structural integrity of *S. aureus* and *E. coli* was severely disrupted after incubating with $AuCu_3$ nanoparticles (10 μg/mL) and H_2O_2 (50 or 100 μM), which was consistent with the plate count experiments, further demonstrating the promising antibacterial activity of $AuCu_3$ nanoparticles.

To demonstrate the antibacterial mechanism of the $AuCu_3$ alloy in the presence of H_2O_2, we conducted additional experiments to measure bacterial membrane permeability, protein leakage, as well as protein and DNA damages resulting from various treatments. The results showed that treatment with $AuCu_3/H_2O_2$ increased bacterial membrane permeability,

https://doi.org/10.1021/acsnano.3c09128
ACS Nano XXXX, XXX, XXX−XXX

as indicated by the significant red fluorescent signals from propidium iodide (PI) that penetrate only damaged cell membranes (Figures S14 and S15). However, there was little change in the red fluorescence signals for those treated with either $AuCu_3$ or H_2O_2 alone, indicating minimal membrane disruptions. Accordingly, the presence of both the $AuCu_3$ alloy and H_2O_2 resulted in a more significant protein leakage from the bacteria, as evidenced by the highest absorbance value at 280 nm in the supernatant of the bacteria compared to other groups (Figure S16). These findings suggest that the bacterial membranes were severely disrupted by the combined treatment of $AuCu_3$ and H_2O_2.[8,13] For DNA and protein damage, treatment with $AuCu_3/H_2O_2$ showed more pronounced effects on *E. coli* than on *S. aureus*. These results suggest a difference in the responses of these two bacteria to $AuCu_3/H_2O_2$ treatment (Figure S17), probably because they have different susceptibility to HO* produced by $AuCu_3$ in the presence of H_2O_2, which is consistent with the antibacterial performances, as shown in Figure 6e and f.

The synthesized $AuCu_3$ nanoparticles exhibited good POD-like activity, low toxicity, and significant antibacterial performances, demonstrating the efficiency of our inverse screening technique in the discovery of antibacterial nanomedicine with enzyme-like activity. The screening method described here depends on the theoretical model for predicting the enzyme-like activity of nanomaterials and thus is adoptable to screen other types of catalytic nanomedicine. For example, catalytic disruption of bacterial quorum sensing to quench bacterial communications has recently emerged as another antimicrobial strategy.[47] This relies on the lactonase-like activity of nanomaterials that facilitates the hydrolysis of N-acylated-L-homoserine lactone (AHL). Once a lactonase-like activity model with computable descriptor(s) has been established, the inverse screening framework can be implemented to identify the appropriate antibacterial nanomedicine. However, it is important to emphasize that the current approach mainly focuses on crucial factors related to antibacterial efficacy. For practical clinical applications, particularly in vivo, many other aspects must also be considered, such as the immune system's response, drug adsorption, distribution, metabolism, and elimination within the body. Due to the limited availability of straightforward parameters for these drug events in vivo, it remains challenging to implement such features in the inverse screening process. This could necessitate the use of artificial intelligence based on big data in the future.[48] Nevertheless, the current screening approach can introduce candidate antibacterial nanomaterials for operating theaters, more efficient aseptic clothes, and similar applications.

CONCLUSIONS

The integrated computational and experimental framework for the inverse screening of antibacterial alloy-nanoparticles without antimicrobial resistance has been constructed and tested. The previously reported POD-like activity model has been verified for metal nanomaterials and implemented to computationally screen the catalytically active alloys from the Material Project library. The previously reported nano-QSAR model was implemented to computationally exclude those with high cytotoxicity. This preliminary computational screening has suggested that $AuCu_3$ should show high POD-like activity and low cytotoxicity. The excellent POD-like activity of $AuCu_3$ over other metals and alloys has been verified in the secondary experimental screening by producing well-defined nanoparticles using SPBCL. Guided by these inverse screening results, $AuCu_3$ nanoparticles have been synthesized in solution, which indeed show good POD-like catalytic activity and antibacterial performances, in particular against Gram-negative *E. coli*. The results have suggested $AuCu_3$ alloys to be a potential antibacterial nanomedicine free from antimicrobial resistance and proved the power of inverse screening in promoting research of nanomedicine. We anticipate that with further development of theoretical models to predict the enzyme-like catalytic abilities of nanomaterials, the present framework can be extended to screen the related enzyme-mimicking alloys for their associated medical applications.

MATERIALS AND METHODS

Models and Computational Details. The crystal structures of 260 binary alloys considered in this work were obtained from the materials project. The optimized bulk crystal structures were used to build slabs, which were then used to generate OH adsorption structures. Slabs were generated automatically using the pymatgen,[49] which ensures a minimum slab size of 8 Å and a vacuum separation of 15 Å along the *z*-direction between two periodically repeated slabs. In geometry optimization of the slabs, the bottom half was fixed.

Periodic density functional theory calculations were performed using the Vienna Ab initio Simulation Package (VASP 5.4.4).[50,51] The Perdew−Burke−Ernzerhof[52] functional with Grimme's semiempirical "D3BJ" dispersion correction[53,54] was employed in these calculations. The plane wave basis sets with an energy cutoff of 450 eV were used to describe valence electrons and the projector-augmented-wave pseudopotentials were used to describe core electrons.[55,56] In geometry optimization of bulk crystal structures, the convergence criteria for energy and atomic force were set to be 10^{-5} eV and 0.02 eV/Å, respectively. For the calculation of hydroxyl adsorption energy, we used a loosen criterion for atomic force, which was set to be 0.05 eV/Å in optimizing slab structures. Such a loosening criterion does not affect the results very much, as shown in Table S8. The Brillouin zone was sampled by a 3 × 3 × 1 Monkhorst−Pack[57] k-point mesh in all calculations of slab models. The adsorption energy of hydroxyl was calculated using eq 2

$$E_{\mathrm{ads,OH}} = E(\mathrm{surface}-\mathrm{OH}) - E(\mathrm{surface}) - E(\mathrm{OH}) \tag{2}$$

where E(surface−OH), E(surface), and E(OH) are energies of the most stable OH-adsorbed surface, separated surface and OH, respectively.

Evaluation of POD-like Activity. It has been shown that the POD-like activity of nanomaterials depends on two key elementary steps, namely H_2O_2 dissociation (step 1) and TMB oxidation (step 2).[26−28] The reaction energies and barriers for these two steps are denoted as $E_{r,i}$ and $E_{b,i}$ (i = 1 or 2), respectively. According to the Bell−Evans−Polanyi (BEP) relation, E_b and E_r show a positive linear relationship for similar reactions; $E_{b,i} = a_i E_{r,i} + b_i$ (i = 1 or 2), where a_i and b_i are constants. Such a linear relationship between $E_{b,i}$ and $E_{r,i}$ (i = 1 or 2) has been demonstrated for iron oxide nanomaterials.[26] The sum of $E_{r,1}$ and $E_{r,2}$ is the reaction energy for TMB oxidation by H_2O_2, which should be a constant irrespective of catalyst. As such, both $E_{b,1}$ and $E_{b,2}$ can be represented with $E_{r,1}$, suggesting that $E_{r,1}$ could serve as a descriptor for the overall reaction. Nevertheless, obtaining $E_{r,1}$ through high-throughput calculations is challenging. Further exploration for simpler descriptors found that $E_{r,1}$ is linearly dependent on hydroxyl adsorption energy ($E_{\mathrm{ads,OH}}$).[26] Therefore, the $E_{\mathrm{ads,OH}}$ value can determine the relative POD-like activity of different nanomaterials, which was employed in our preliminary computational screening. The Python scripts for high-throughput $E_{\mathrm{ads,OH}}$ calculation can be accessed through https://github.com/xingfagao/PyPOD.

Evaluation of Cytotoxicity. The quantitative structure−activity relationship model for nanomaterials (Nano-QSAR$_{\mathrm{mix}}$) was used to evaluate the cytotoxicity of different alloys, where the physical descriptor was chosen as the covalent radius (R_c).[31] For alloy systems, the descriptor was represented as an additive mixture ($R_{c,\mathrm{mix}}$) of composition-weighted descriptors for individual metals.[58,59] The $R_{c,mix}$ can be calculated using eq 3

$$R_{c,mix} = \frac{x}{x+y}R_{c,A} + \frac{y}{x+y}R_{c,B} \tag{3}$$

where $R_{c,A}$ and $R_{c,B}$ are covalent radii[60] of metal species A and B in the binary alloy A_xB_y. The cytotoxicity was represented by the logarithm of 50% inhibition of the cell viability (pEC_{50}), which can be calculated using eq 4

$$pEC_{50} = 4.641 + 0.0013R_{c,mix} \tag{4}$$

It should be noted that the above Nano-$QSAR_{mix}$ model was developed to evaluate the cytotoxicity of TiO_2-supported alloy systems. Thus, the predicted cytotoxicities in this work represent relative values for alloys of the same quantity. To ensure the validity of the model, the cytotoxicity presented in this work was evaluated for different alloys loaded with a molar fraction of 5% on TiO_2.

Materials. Poly(ethylene oxide)-*block*-poly(2-vinylpyridine) (PEO-*b*-P2VP, M_n = 2.8-*b*-1.5 kg/mol, polydispersity index = 1.11) was purchased from Polymer Source, Inc. Hexamethyl disilazane (HMDS) was obtained from Marklin. $HAuCl_4 \cdot 3H_2O$, $H_2PtCl_6 \cdot 6H_2O$, polyvinylpyrrolidone (PVP, M_w 55000), and sodium borohydride were obtained from Sigma−Aldrich. $AgNO_3$, $Cu(NO_3)_2 \cdot xH_2O$, $Ni(NO_3)_2 \cdot 6H_2O$, $IrCl_3$, $RuCl_3$, and $Pd(NO_3)_2 \cdot 2H_2O$ were purchased from Adamas. 3,3′,5,5′-Tetramethylbenzidine (TMB), sodium acetate (NaOAc), and cupric acetate monohydrate ($Cu(CH_3COO)_2 \cdot H_2O$) were purchased from Aladdin Chemical Co., Ltd. Silicon wafers were obtained from Lijingkeji. Silicon nitride films were purchased from Suzhou in situ chips. Polydimethylsiloxane (PDMS) tip arrays were obtained from TERA-print. All the chemical reagents were of analytical grade and were used without any further purification. The deionized (DI) water of resistivity ≥18.2 MΩ was used in all experiments.

Instrumentation. SPBCL was conducted by using a Tera-Fab M series. The imprinted metal-containing polymer feature (i.e., nanoreactor) arrays were characterized using an optical microscope (Nikon, H600L). Thermal reduction of the imprinted nanoreactor arrays was conducted in a tube furnace (GMF-2Z, BEQ). The obtained nanoparticles were characterized using a scanning electron microscope (SEM, S4800) and an aberration corrected transmission electron microscope (AC-TEM, Themis Z). The morphologies of the bacteria were observed by scanning electron microscopy (SEM, Zeiss Ultra 55 microscope). Inductively coupled plasma-optical emission spectroscopy (ICP−OES) measurements were performed on an Agilent 5110 analyzer. Powder X-ray diffraction (XRD) patterns were measured by a Rigaku Ultima diffractometer at 5°/min using Cu Kα radiation. Absorption spectra were collected using a microplate reader (Molecular Device, USA). Steady-state kinetic assays were carried out on a spectrophotometer (UV-3600 Plus, Shimadzu).

Synthesis of (Alloy) Nanoparticle Arrays Based on SPBCL. To make up the metal-containing ink, PEO-*b*-P2VP was first dissolved in DI water at a concentration of 5 mg/mL until there was no obvious solid precipitate in the solution. Subsequently, an aqueous solution of the metal precursor was added to control the ratio of metal ions to the amount of pyridine in the block copolymer between 1:32 and 1:128. The mixture was then placed in a shaker for 24 h at room temperature. To improve the hydrophilicity, the PDMS tip array was treated with oxygen plasma (150 W, 2 min). Following that, 200 μL of the ink solution was drop cast in the middle of the tip array and allowed to dry under a low-humidity environment before use.

Silicon nitride films and silicon wafers were used as substrates for subsequent transmission electron microscopy characterization and POD-like measurements, respectively. Prior to patterning, these substrates were placed in a closed chamber with vials containing HMDS at room temperature for 48 h to allow for HMDS vapor deposition to improve the hydrophobicity of the substrates. The inked PDMS tip array and the silicon wafer substrate were then mounted to the Tera-Fab instrument, which were aligned according to the shape change of the tips observed using a microscope. The patterning was performed under a relative humidity of *ca.* 90% to facilitate the transfer of ink. The contact force was kept at 100 mN. The as-resulted substrate with printed nanoreactor arrays was placed in a tube furnace and heated first at 150 °C for 12 h under Ar and then at 500 °C for 12 h under H_2.

Synthesis of $AuCu_3$ Nanoparticles via a Solution Phase Method. The $AuCu_3$ nanoparticles were synthesized according to previous methods[46] with a minor modification. First, 10.1 mg of $Cu(CH_3COO)_2 \cdot H_2O$ and 6.7 mg of $HAuCl_4 \cdot 3H_2O$ were dissolved in 25 mL of deionized water, and the mixture was stirred under Ar for 20 min. Then, 10 mL of a 0.05 M $NaBH_4$ solution was injected into the above mixture under stirring. The solution color gradually changed from dark red to dark brown, suggesting the formation of Au and Cu aggregate structures. After stirring for 2 h, the resulting product ($AuCu_3$ precursors) was centrifuged and washed with acetone, which was then dried under vacuum at 50 °C for overnight. The precursor powder was finally annealed at 300 °C in N_2 for 2 h with a ramp rate of 5 °C/min to obtain the final $AuCu_3$ nanoparticles.

POD-like Activity Measurements. To determine the POD-like activity of nanoparticle arrays prepared by SPBCL, 100 μL of 1 M H_2O_2, 100 μL of 10 mM TMB, and nanoparticles loaded on a silicon wafer were added to 800 μL of 200 mM acetate buffer solution (pH 4.5). The final concentrations of H_2O_2 and TMB were 100 and 0.5 mM, respectively. After mixing for 20 min, the reaction solution was used for UV−visible spectroscopic measurements, and the relative catalytic capacities of these nanozymes were calculated as follows:

$$\text{Relative catalytic capacity} = \frac{A_{\text{with nanozymes,650 nm}} - A_{\text{blank,650 nm}}}{A_{\text{control,650 nm}} - A_{\text{blank,650 nm}}} \tag{5}$$

where A_{blank} is the absorbance at 650 nm in the presence of TMB in acetate buffer solution, and $A_{control}$ is the absorbance at 650 nm in the presence of H_2O_2 and TMB in acetate buffer solution.

Steady-State Kinetics Assays for $AuCu_3$ Nanoparticles. The POD-like activity of $AuCu_3$ prepared by a solution phase method was evaluated by steady-state kinetics assays. Briefly, assays were conducted using H_2O_2 as a substrate. A 0.2 M NaOAc buffer solution (pH 4.0) was used as the reaction buffer, and 5 μg/mL $AuCu_3$ was used for the kinetics assays. The kinetic data were obtained by varying the concentration of H_2O_2 while keeping the TMB concentration constant. Nanozymes were mixed with different concentrations of H_2O_2 in the buffer solution, and the absorbance of the reaction solution at 652 nm was immediately measured. Then, the "Absorbance vs Time" curve was obtained, which can be used to calculate the initial reaction velocity (ν). The kinetics constants (i.e., ν_{max} and K_m) were calculated by fitting the reaction velocity values and the substrate concentrations to the Michaelis−Menten equation as follows:

$$\nu = \frac{\nu_{max}[S]}{K_m + [S]} \tag{6}$$

where ν is the initial reaction velocity, $[S]$ is the substrate concentration, K_m is the Michaelis constant, and ν_{max} is the maximal reaction velocity. The values of K_m and ν_{max} can be calculated from the double reciprocal plots of eq 6.

Electron Spin Resonance Analysis of *OH Formation. Glass capillary tubes containing nanozymes (10 μg/mL), H_2O_2 (100 μM), DMPO (10 mM), and HAc-NaAc buffer (0.1 M, pH 4.5) were inserted into the electron paramagnetic resonance cavity to record *OH signals after 5 min of reaction.

Cytotoxicities of $AuCu_3$ Nanoparticles. RAW 264.7 cells were acquired from the cell bank of the Chinese Academy of Sciences (Shanghai, China). Cells were cultured in high-glucose Dulbecco's modified Eagle's (DMEM) medium (Bio-Channel, China) containing 10% (v/v) fetal bovine serum and 1% penicillin/streptomycin in a humidified 5% CO_2 atmosphere at 37 °C. To assess the cell viability, Raw 264.7 cells were seeded into 96-well plates with a density of 5 × 10^3 cells per well. The medium was refreshed after overnight incubation, followed by addition of various formulations of $AuCu_3$

with different concentrations (0−100 μg/mL). Following the incubation for another 24 h, the cells were washed with PBS three times. Cell viability was determined by a CCK (Cell Counting Kit)-8 assay ($n = 5$), according to the manufacturer's instructions by using a SpectraMax M2e (Molecular Device, USA) microplate reader.

TA Assays. For fluorescence measurements, various concentrations (10, 20, and 40 μg/mL) of $AuCu_3$, 1 mM H_2O_2, and 4 mM TA were reacted for 30 min. The fluorescent product of TAOH was monitored by using a fluorescence spectrophotometer under excitation wavelength of 315 nm.

Antibacterial Activities of $AuCu_3$ Nanoparticles. The antibacterial activities of $AuCu_3$ nanoparticles were evaluated via the number of colony-forming units (CFU) by using the plate count experiments. The antibacterial experiments were divided into four groups: (1) bacteria + NaAc-HAc buffer; (2) bacteria + H_2O_2; (3) bacteria + $AuCu_3$ nanozymes (10 μg/mL); and (4) bacteria + H_2O_2 + $AuCu_3$ nanozymes (10 μg/mL). The concentration of H_2O_2 was 100 μM for *E. coli* and 50 μM for *S. aureus*. *E. coli* and *S. aureus* were cultured overnight in Luria−Bertani medium at 37 °C in an incubator shaker. When the absorbance value of the bacterial solution was 0.7−0.8, the bacteria were diluted 10 times with phosphate buffered saline (PBS), and 100 μL of diluted bacteria was added into a 1.5 mL centrifuge tube. The bacteria were collected by centrifugation and resuspended in a NaAc-HAc buffer (0.1 M, pH 5.0). The final concentration of the prepared bacterial solution was 1.0×10^6-1.0×10^7 CFU/mL in NaAc-HAc buffer. The mixed suspension was then incubated with the above different groups for 3 h at 37 °C in an incubator shaker. After treatment, 20 μL of the above suspension was spread evenly on solid agar medium and cultured for 12 h at 37 °C for CFU enumeration. 100 μL of suspension was spread evenly on solid agar medium for taking photographs of colonies after different treatments.

Morphological Characterization of Bacteria by SEM. The bacteria with different treatments were rinsed with saline. The suspensions were then centrifuged and redispersed in 2.5% glutaraldehyde for 4 h at 4 °C under dark conditions. Different concentrations of ethanol (30%, 50%, 70%, 80%, 90%, and 100%) were used to dehydrate the cells for 10 min, respectively. At last, SEM experiments were performed to visualize the morphological changes of bacteria.

DNA Damage. The *E. coli* and S. aureus were treated with (1) 0.1 M NaAc (control), (2) H_2O_2, (3) $AuCu_3$, and (4) $AuCu_3$+H_2O_2 for 3 h. Genomic DNA from *E. coli* and *S. aureus* was then collected and processed by using a TaKaRa MiniBEST bacteria Genomic DNA Extraction Kit v3.0 (TaKaRa, Japan), and finally identified using agarose gel electrophoresis with goldview nucleic acid gel stain.

Membrane Permeability Disruption. Bacterial suspensions treated with (1) 0.1 M NaAc (control), (2) H_2O_2, (3) $AuCu_3$, and (4) $AuCu_3$+H_2O_2 for 3 h were collected by centrifugation at 4000 rpm for 5 min. The cells were then stained with SYTO 9 and propidium iodide (PI) for 15 min and visualized via confocal fluorescence microscope (Olympus, Japan).

Protein Leakage and Damage. The *E. coli* and *S. aureus* were treated with (1) 0.1 M NaAc (control), (2) H_2O_2, (3) $AuCu_3$, and (4) $AuCu_3$+H_2O_2 for 3 h by centrifugation at 4000 rpm for 5 min to collect supernatants and precipitates, respectively. The absorbance value at 280 nm of supernatants was detected to evaluate bacterial protein leakage using one drop (Wins Technology Co., Ltd., Nanjing, China). For the experiments of protein damage, the precipitates were processed using Bacterial Activity-Keeping Lysis Buffer (Sangon Biotech Co., Ltd., Shanghai, China). After that, the loading buffer containing SDS (10% w/v), acrylamide (30% w/v), Tris-HCl buffer (1.5 M, pH 8.8 or 1.0 M, pH 6.8), ammonium persulfate (10% w/v), and bromophenol blue (0.01% w/v) were added. The protein solutions were then denatured by boiling for 10 min and also analyzed with SDS-PAGE by a GelDoc EZ Imager (Bio-Rad).

ASSOCIATED CONTENT

Supporting Information

The Supporting Information is available free of charge at https://pubs.acs.org/doi/10.1021/acsnano.3c09128.

> List of binary alloys and their cytotoxicities, distribution of DFT-calculated $E_{ads,OH}$, additional characterization data of $AuCu_3$ and peroxidase-like activities, corresponding tables and photographs for comparison of antibacterial performances (PDF)

AUTHOR INFORMATION

Corresponding Authors

Yi-Ge Zhou − *Institute of Chemical Biology and Nanomedicine (ICBN), State Key Laboratory of Chemo/Biosensing and Chemometrics, College of Chemistry and Chemical Engineering, Hunan University, Changsha 410082, P. R. China*; orcid.org/0000-0002-4155-7222; Email: yigezhou@hnu.edu.cn

Hui Wei − *Department of Biomedical Engineering, College of Engineering and Applied Sciences, Nanjing National Laboratory of Microstructures, Jiangsu Key Laboratory of Artificial Functional Materials, Chemistry and Biomedicine Innovation Center (ChemBIC), Nanjing University, Nanjing 210023, P. R. China*; orcid.org/0000-0003-0870-7142; Email: weihui@nju.edu.cn

Xingfa Gao − *Laboratory of Theoretical and Computational Nanoscience, National Center for Nanoscience and Technology, Chinese Academy of Sciences, Beijing 100190, P. R. China*; orcid.org/0000-0002-1636-6336; Email: gaoxf@nanoctr.cn

Authors

Jia-Jia Zheng − *Laboratory of Theoretical and Computational Nanoscience, National Center for Nanoscience and Technology, Chinese Academy of Sciences, Beijing 100190, P. R. China*; orcid.org/0000-0002-6040-6219

Xiaoyu Wang − *Department of Biomedical Engineering, College of Engineering and Applied Sciences, Nanjing National Laboratory of Microstructures, Jiangsu Key Laboratory of Artificial Functional Materials, Chemistry and Biomedicine Innovation Center (ChemBIC), Nanjing University, Nanjing 210023, P. R. China; Department of Chemistry and Material Science, College of Science, Nanjing Forestry University, Nanjing 210037, P. R. China*; orcid.org/0000-0002-8641-2430

Zeqi Li − *Institute of Chemical Biology and Nanomedicine (ICBN), State Key Laboratory of Chemo/Biosensing and Chemometrics, College of Chemistry and Chemical Engineering, Hunan University, Changsha 410082, P. R. China*

Xiaomei Shen − *Key Laboratory of Functional Small Organic Molecule, College of Chemistry and Chemical Engineering, Jiangxi Normal University, Nanchang 330022, P. R. China*; orcid.org/0000-0002-7851-9959

Gen Wei − *Department of Biomedical Engineering, College of Engineering and Applied Sciences, Nanjing National Laboratory of Microstructures, Jiangsu Key Laboratory of Artificial Functional Materials, Chemistry and Biomedicine Innovation Center (ChemBIC), Nanjing University, Nanjing 210023, P. R. China*

Pufeihong Xia − *Institute of Chemical Biology and Nanomedicine (ICBN), State Key Laboratory of Chemo/*

Biosensing and Chemometrics, College of Chemistry and Chemical Engineering, Hunan University, Changsha 410082, P. R. China

Complete contact information is available at:
https://pubs.acs.org/10.1021/acsnano.3c09128

Author Contributions

†J.-J. Z., X. W., and Z.-Q. L. contributed equally. The manuscript was written through the contributions of all authors. All authors have given approval to the final version of the manuscript.

Notes

The authors declare no competing financial interest.

ACKNOWLEDGMENTS

This work was supported by the National Key Research and Development Program of China (2022YFA1207300), Natural Science Foundation of China (22203020, 52161135107, 22007041, 22367013), Science and Technology Foundation of Jiangxi Educational Department (GJJ191701) and Natural Science Foundation of Jiangxi Province (20212BAB213019).

REFERENCES

(1) Yacoby, I.; Benhar, I. Antibacterial Nanomedicine. *Nanomedicine* **2008**, *3*, 329−341.

(2) Wang, J.; Li, Y.; Nie, G.; Zhao, Y. Precise Design of Nanomedicines: Perspectives for Cancer Treatment. *Natl. Sci. Rev.* **2019**, *6*, 1107−1110.

(3) Nadeem, S.; Chen, Z.; Wei, M.; Li, F.; Ling, D. Nanomedicine-Induced Pyroptosis for Cancer Therapy. *Nanomedicine* **2021**, *16*, 1071−1074.

(4) Mitchell, M. J.; Billingsley, M. M.; Haley, R. M.; Wechsler, M. E.; Peppas, N. A.; Langer, R. Engineering Precision Nanoparticles for Drug Delivery. *Nat. Rev. Drug Discovery* **2021**, *20*, 101−124.

(5) Bhatia, S. N.; Chen, X.; Dobrovolskaia, M. A.; Lammers, T. Cancer Nanomedicine. *Nat. Rev. Cancer* **2022**, *22*, 550−556.

(6) Gupta, A.; Mumtaz, S.; Li, C.-H.; Hussain, I.; Rotello, V. M. Combatting Antibiotic-Resistant Bacteria Using Nanomaterials. *Chem. Soc. Rev.* **2019**, *48*, 415−427.

(7) Makabenta, J. M. V.; Nabawy, A.; Li, C.-H.; Schmidt-Malan, S.; Patel, R.; Rotello, V. M. Nanomaterial-Based Therapeutics for Antibiotic-Resistant Bacterial Infections. *Nat. Rev. Microbiol.* **2021**, *19*, 23−36.

(8) Xie, M.; Gao, M.; Yun, Y.; Malmsten, M.; Rotello, V. M.; Zboril, R.; Akhavan, O.; Kraskouski, A.; Amalraj, J.; Cai, X.; et al. Antibacterial Nanomaterials: Mechanisms, Impacts on Antimicrobial Resistance and Design Principles. *Angew. Chem., Int. Ed.* **2023**, *62*, No. e202217345.

(9) Xin, Q.; Shah, H.; Nawaz, A.; Xie, W.; Akram, M. Z.; Batool, A.; Tian, L.; Jan, S. U.; Boddula, R.; Guo, B.; Liu, Q.; Gong, J. R. Antibacterial Carbon-Based Nanomaterials. *Adv. Mater.* **2019**, *31*, 1804838.

(10) Makvandi, P.; Wang, C.; Zare, E. N.; Borzacchiello, A.; Niu, L.; Tay, F. R. Metal-Based Nanomaterials in Biomedical Applications: Antimicrobial Activity and Cytotoxicity Aspects. *Adv. Funct. Mater.* **2020**, *30*, 1910021.

(11) Wang, Y.; Yang, Y.; Shi, Y.; Song, H.; Yu, C. Antibiotic-Free Antibacterial Strategies Enabled by Nanomaterials: Progress and Perspectives. *Adv. Mater.* **2020**, *32*, 1904106.

(12) Mei, L.; Zhu, S.; Liu, Y.; Yin, W.; Gu, Z.; Zhao, Y. An Overview of the Use of Nanozymes in Antibacterial Applications. *Chem. Eng. J.* **2021**, *418*, 129431.

(13) Jin, L.; Cao, F.; Gao, Y.; Zhang, C.; Qian, Z.; Zhang, J.; Mao, Z. Microenvironment-Activated Nanozyme-Armed Bacteriophages Efficiently Combat Bacterial Infection. *Adv. Mater.* **2023**, *35*, 2301349.

(14) Magiorakos, A. P.; Srinivasan, A.; Carey, R. B.; Carmeli, Y.; Falagas, M. E.; Giske, C. G.; Harbarth, S.; Hindler, J. F.; Kahlmeter, G.; Olsson-Liljequist, B.; Paterson, D. L.; Rice, L. B.; Stelling, J.; Struelens, M. J.; Vatopoulos, A.; Weber, J. T.; Monnet, D. L. Multidrug-Resistant, Extensively Drug-Resistant and Pandrug-Resistant Bacteria: An International Expert Proposal for Interim Standard Definitions for Acquired Resistance. *Clin. Microbiol. Infect.* **2012**, *18*, 268−281.

(15) Bassetti, M.; Merelli, M.; Temperoni, C.; Astilean, A. New Antibiotics for Bad Bugs: Where Are We? *Ann. Clin. Microbiol. Antimicrob.* **2013**, *12*, 22.

(16) Hassan Baig, M.; Ahmad, K.; Roy, S.; Mohammad Ashraf, J.; Adil, M.; Haris Siddiqui, M.; Khan, S.; Amjad Kamal, M.; Provaznik, I.; Choi, I. Computer Aided Drug Design: Success and Limitations. *Curr. Pharm. Des.* **2016**, *22*, 572−581.

(17) Maren, T. H. The Development of Topical Carbonic Anhydrase Inhibitors. *J. Glaucoma* **1995**, *4*, 49−62.

(18) Perry, C. M.; Benfield, P. Nelfinavir. *Drugs* **1997**, *54*, 81−87.

(19) Monto, A. S.; Robinson, D. P.; Herlocher, M. L.; Hinson, J. M., Jr.; Elliott, M. J.; Crisp, A. Zanamivir in the Prevention of Influenza among Healthy Adults: A Randomized Controlled Trial. *JAMA* **1999**, *282*, 31−35.

(20) Tran, K.; Ulissi, Z. W. Active Learning across Intermetallics to Guide Discovery of Electrocatalysts for CO_2 Reduction and H_2 Evolution. *Nat. Catal.* **2018**, *1*, 696−703.

(21) Wen, Y.; Fu, L.; Li, G.; Ma, J.; Ma, H. Accelerated Discovery of Potential Organic Dyes for Dye-Sensitized Solar Cells by Interpretable Machine Learning Models and Virtual Screening. *Sol. RRL* **2020**, *4*, 2000110.

(22) Zhang, S.; Lu, S.; Zhang, P.; Tian, J.; Shi, L.; Ling, C.; Zhou, Q.; Wang, J. Accelerated Discovery of Single-Atom Catalysts for Nitrogen Fixation Via Machine Learning. *Energy Environ. Mater.* **2023**, *6*, No. e12304.

(23) Jain, A.; Ong, S. P.; Hautier, G.; Chen, W.; Richards, W. D.; Dacek, S.; Cholia, S.; Gunter, D.; Skinner, D.; Ceder, G.; Persson, K. A. Commentary: The Materials Project: A Materials Genome Approach to Accelerating Materials Innovation. *APL Mater.* **2013**, *1*, 011002.

(24) Ong, S. P.; Cholia, S.; Jain, A.; Brafman, M.; Gunter, D.; Ceder, G.; Persson, K. A. The Materials Application Programming Interface (API): A Simple, Flexible and Efficient API for Materials Data Based on Representational State Transfer (REST) Principles. *Comput. Mater. Sci.* **2015**, *97*, 209−215.

(25) Nakaya, Y.; Furukawa, S. Catalysis of Alloys: Classification, Principles, and Design for a Variety of Materials and Reactions. *Chem. Rev.* **2023**, *123*, 5859−5947.

(26) Shen, X.; Wang, Z.; Gao, X.; Zhao, Y. Density Functional Theory-Based Method to Predict the Activities of Nanomaterials as Peroxidase Mimics. *ACS Catal.* **2020**, *10*, 12657−12665.

(27) Gao, X. J.; Zhao, Y.; Gao, X. Catalytic Signal Transduction Theory Enabled Virtual Screening of Nanomaterials for Medical Functions. *Acc. Chem. Res.* **2023**, *56*, 2366−2377.

(28) Shen, X.; Wang, Z.; Gao, X. J.; Gao, X. Reaction Mechanisms and Kinetics of Nanozymes: Insights from Theory and Computation. *Adv. Mater.* **2023**, 2211151.

(29) Puzyn, T.; Rasulev, B.; Gajewicz, A.; Hu, X.; Dasari, T. P.; Michalkova, A.; Hwang, H.-M.; Toropov, A.; Leszczynska, D.; Leszczynski, J. Using Nano-QSAR to Predict the Cytotoxicity of Metal Oxide Nanoparticles. *Nat. Nanotechnol.* **2011**, *6*, 175−178.

(30) Mikolajczyk, A.; Sizochenko, N.; Mulkiewicz, E.; Malankowska, A.; Rasulev, B.; Puzyn, T. A Chemoinformatics Approach for the Characterization of Hybrid Nanomaterials: Safer and Efficient Design Perspective. *Nanoscale* **2019**, *11*, 11808−11818.

(31) Roy, J.; Ojha, P. K.; Roy, K. Risk Assessment of Heterogeneous TiO_2-Based Engineered Nanoparticles (NPs): A QSTR Approach Using Simple Periodic Table Based Descriptors. *Nanotoxicology* **2019**, *13*, 701−716.

(32) Gao, L.; Zhuang, J.; Nie, L.; Zhang, J.; Zhang, Y.; Gu, N.; Wang, T.; Feng, J.; Yang, D.; Perrett, S.; Yan, X. Intrinsic Peroxidase-

Like Activity of Ferromagnetic Nanoparticles. *Nat. Nanotechnol.* **2007**, *2*, 577−583.

(33) Wu, J.; Wang, X.; Wang, Q.; Lou, Z.; Li, S.; Zhu, Y.; Qin, L.; Wei, H. Nanomaterials with Enzyme-Like Characteristics (Nanozymes): Next-Generation Artificial Enzymes (II). *Chem. Soc. Rev.* **2019**, *48*, 1004−1076.

(34) Ma, C.-B.; Xu, Y.; Wu, L.; Wang, Q.; Zheng, J.-J.; Ren, G.; Wang, X.; Gao, X.; Zhou, M.; Wang, M.; Wei, H. Guided Synthesis of a Mo/Zn Dual Single-Atom Nanozyme with Synergistic Effect and Peroxidase-Like Activity. *Angew. Chem., Int. Ed.* **2022**, *61*, No. e202116170.

(35) Fan, J.; Yin, J.-J.; Ning, B.; Wu, X.; Hu, Y.; Ferrari, M.; Anderson, G. J.; Wei, J.; Zhao, Y.; Nie, G. Direct Evidence for Catalase and Peroxidase Activities of Ferritin-Platinum Nanoparticles. *Biomaterials* **2011**, *32*, 1611−1618.

(36) Cui, M.; Zhou, J.; Zhao, Y.; Song, Q. Facile Synthesis of Iridium Nanoparticles with Superior Peroxidase-Like Activity for Colorimetric Determination of H_2O_2 and Xanthine. *Sens. Actuators, B* **2017**, *243*, 203−210.

(37) Rastogi, L.; Kumar Sashidhar, R. B.; Karunasagar, D.; Giri, A. Peroxidase-Like Activity of Gum Kondagogu Reduced/Stabilized Palladium Nanoparticles and Its Analytical Application for Colorimetric Detection of Glucose in Biological Samples. *Sens. Actuators, B* **2017**, *240*, 1182−1188.

(38) Cao, G.-J.; Jiang, X.; Zhang, H.; Croley, T. R.; Yin, J.-J. Mimicking Horseradish Peroxidase and Oxidase Using Ruthenium Nanomaterials. *RSC Adv.* **2017**, *7*, 52210−52217.

(39) Shah, J.; Singh, S. Unveiling the Role of Atp in Amplification of Intrinsic Peroxidase-Like Activity of Gold Nanoparticles. *3 Biotech* **2018**, *8*, 67.

(40) Zaka, M.; Abbasi, B. H. Effects of Bimetallic Nanoparticles on Seed Germination Frequency and Biochemical Characterisation of Eruca Sativa. *IET Nanobiotechnol.* **2017**, *11*, 255−260.

(41) Chai, J.; Huo, F.; Zheng, Z.; Giam, L. R.; Shim, W.; Mirkin, C. A. Scanning Probe Block Copolymer Lithography. *Proc. Natl. Acad. Sci. U.S.A.* **2010**, *107*, 20202−20206.

(42) Liu, G.; Eichelsdoerfer, D. J.; Rasin, B.; Zhou, Y.; Brown, K. A.; Liao, X.; Mirkin, C. A. Delineating the Pathways for the Site-Directed Synthesis of Individual Nanoparticles on Surfaces. *Proc. Natl. Acad. Sci. U.S.A.* **2013**, *110*, 887−891.

(43) Chen, P.-C.; Liu, G.; Zhou, Y.; Brown, K. A.; Chernyak, N.; Hedrick, J. L.; He, S.; Xie, Z.; Lin, Q.-Y.; Dravid, V. P.; O'Neill-Slawecki, S. A.; Mirkin, C. A. Tip-Directed Synthesis of Multimetallic Nanoparticles. *J. Am. Chem. Soc.* **2015**, *137*, 9167−9173.

(44) Chen, P.-C.; Liu, X.; Hedrick, J. L.; Xie, Z.; Wang, S.; Lin, Q.-Y.; Hersam, M. C.; Dravid, V. P.; Mirkin, C. A. Polyelemental Nanoparticle Libraries. *Science* **2016**, *352*, 1565−1569.

(45) Huang, L.; Chen, P.-C.; Liu, M.; Fu, X.; Gordiichuk, P.; Yu, Y.; Wolverton, C.; Kang, Y.; Mirkin, C. A. Catalyst Design by Scanning Probe Block Copolymer Lithography. *Proc. Natl. Acad. Sci. U.S.A.* **2018**, *115*, 3764−3769.

(46) Sra, A. K.; Schaak, R. E. Synthesis of Atomically Ordered AuCu and $AuCu_3$ Nanocrystals from Bimetallic Nanoparticle Precursors. *J. Am. Chem. Soc.* **2004**, *126*, 6667−6672.

(47) Gao, M.; Xu, B.; Huang, Y.; Cao, J.; Yang, L.; Liu, X.; Djumaev, A.; Wu, D.; Shoxiddinova, M.; Cai, X.; et al. Nano-Enabled Quenching of Bacterial Communications for the Prevention of Biofilm Formation. *Angew. Chem., Int. Ed.* **2023**, *62*, No. e202305485.

(48) Ho, D. Digital Nanomedicine: A New Frontier for Drug Development. *ACS Nano* **2022**, *16*, 3435−3437.

(49) Ong, S. P.; Richards, W. D.; Jain, A.; Hautier, G.; Kocher, M.; Cholia, S.; Gunter, D.; Chevrier, V. L.; Persson, K. A.; Ceder, G. Python Materials Genomics (Pymatgen): A Robust, Open-Source Python Library for Materials Analysis. *Comput. Mater. Sci.* **2013**, *68*, 314−319.

(50) Kresse, G.; Furthmuller, J. Efficient Iterative Schemes for Ab Initio Total-Energy Calculations Using a Plane-Wave Basis Set. *Phys. Rev. B* **1996**, *54*, 11169−11186.

(51) Kresse, G.; Furthmuller, J. Efficiency of Ab-Initio Total Energy Calculations for Metals and Semiconductors Using a Plane-Wave Basis Set. *Comput. Mater. Sci.* **1996**, *6*, 15−50.

(52) Perdew, J. P.; Burke, K.; Ernzerhof, M. Generalized Gradient Approximation Made Simple. *Phys. Rev. Lett.* **1996**, *77*, 3865−3868.

(53) Grimme, S.; Antony, J.; Ehrlich, S.; Krieg, H. A Consistent and Accurate Ab Initio Parametrization of Density Functional Dispersion Correction (DFT-D) for the 94 Elements H-Pu. *J. Chem. Phys.* **2010**, *132*, 154104.

(54) Grimme, S.; Ehrlich, S.; Goerigk, L. Effect of the Damping Function in Dispersion Corrected Density Functional Theory. *J. Comput. Chem.* **2011**, *32*, 1456−1465.

(55) Blochl, P. E. Projector Augmented-Wave Method. *Phys. Rev. B* **1994**, *50*, 17953−17979.

(56) Kresse, G.; Joubert, D. From Ultrasoft Pseudopotentials to the Projector Augmented-Wave Method. *Phys. Rev. B* **1999**, *59*, 1758−1775.

(57) Monkhorst, H. J.; Pack, J. D. Special Points for Brillouin-Zone Integrations. *Phys. Rev. B* **1976**, *13*, 5188−5192.

(58) Walker, J. D.; Jaworska, J.; Comber, M. H.; Schultz, T. W.; Dearden, J. C. Guidelines for Developing and Using Quantitative Structure-Activity Relationships. *Environ. Toxicol. Chem.* **2003**, *22*, 1653−65.

(59) Muratov, E. N.; Varlamova, E. V.; Artemenko, A. G.; Polishchuk, P. G.; Kuz'min, V. E. Existing and Developing Approaches for QSAR Analysis of Mixtures. *Mol. Inf.* **2012**, *31*, 202−221.

(60) Cordero, B.; Gomez, V.; Platero-Prats, A. E.; Reves, M.; Echeverria, J.; Cremades, E.; Barragan, F.; Alvarez, S. Covalent Radii Revisited. *Dalton Trans.* **2008**, 2832−2838.